Journal Pre-proof

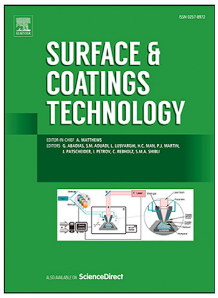

Optical anisotropy of nanostructured vanadium dioxide thermochromic thin films synthesized by reactive magnetron sputtering combined with glancing angle deposition

G. Savorianakis, C. Rousseau, Y. Battie, A. En Naciri, B. Maes, M. Voué, S. Konstantinidis

PII: S0257-8972(25)00212-9
DOI: https://doi.org/10.1016/j.surfcoat.2025.131938
Reference: SCT 131938

To appear in: *Surface & Coatings Technology*

Received date : 25 November 2024
Revised date : 13 February 2025
Accepted date : 15 February 2025

Graphical Abstract

Optical anisotropy of nanostructured vanadium dioxide thermochromic thin films synthesized by reactive magnetron sputtering combined with glancing angle deposition

G. Savorianakis, C. Rousseau, Y. Battie, A. En Naciri, B. Maes, M. Voué, S. Konstantinidis

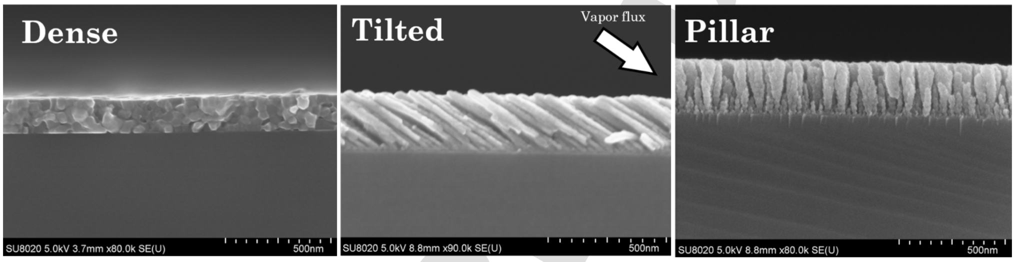

Highlights

Optical anisotropy of nanostructured vanadium dioxide thermochromic thin films synthesized by reactive magnetron sputtering combined with glancing angle deposition

G. Savorianakis, C. Rousseau, Y. Battie, A. En Naciri, B. Maes, M. Voué, S. Konstantinidis

- High purity anisotropic and thermochromic VO_2 nanostructured thin films, including tilted and pillar-like morphologies, were prepared by GLAD technique
- These tilted and pillar-like morphologies markedly enhance the thermochromic behaviour of the films
- Optical characterization using azimuthal Mueller matrix measurements reveals a strong correlation between nanostructure geometry and optical anisotropy
- Finite element simulations and modelling approaches such as the Berreman 4x4 transfer matrix method provide valuable insights into the behaviour of these nanostructures.

Optical anisotropy of nanostructured vanadium dioxide thermochromic thin films synthesized by reactive magnetron sputtering combined with glancing angle deposition

G. Savorianakis[a], C. Rousseau[b], Y. Battie[c], A. En Naciri[c], B. Maes[b], M. Voué[d], S. Konstantinidis[a]

[a]*Plasma-Surface Interaction Chemistry (ChIPS), Research Institute for Materials Science and Engineering, University of Mons, Place du Parc, 20, Mons, B-7000, Belgium*
[b]*Micro- and Nanophotonic Materials Group (MMNP), Research Institute for Materials Science and Engineering, University of Mons, Place du Parc, 20, Mons, B-7000, Belgium*
[c]*Laboratoire de chimie et physique – Approche multi-échelle des milieux complexes (LCP-A2MC), University of Lorraine, Boulevard Dominique François Arago, 1, Metz Technopole, 57070, France*
[d]*Physics of Materials and Optics Group (LPMO), Research Institute for Materials Science and Engineering, University of Mons, , Place du Parc, 20, Mons, B-7000, Belgium*

Abstract

In this study, we explore the optical and thermochromic properties of monoclinic vanadium dioxide (VO_2) nanostructures, which undergo a reversible phase transition from an insulating to a metallic state at around 68 °C. This phase transition is crucial for applications such as photonic devices, tunable optical filters, and energy-efficient windows. While the performance of VO_2 can be optimized by tailoring its nanostructure and film morphology, to the best of our knowledge, no prior work in the literature has successfully synthesized VO_2 nanostructures with well-defined morphology and high VO_2 purity using the Glancing Angle Deposition (GLAD) technique.

In this work, by combining reactive magnetron sputtering of a vanadium target in an Argon-Oxygen atmosphere with GLancing Angle Deposition (GLAD), we synthesized thin films of VO_2, followed by post-deposition annealing in an oxygen-rich environment. Through GLAD we elaborate anisotropic nanostructures, including tilted and straight columns morphologies. Optical characterizations techniques, such as ellipsometric measurements and grazing incidence X-ray diffraction (GIXRD), were employed to evaluate the crystalline phase and dielectric functions of the films in both their metallic and insulating states. For the tilted nanocolumns, azimuthal Mueller matrix measurements reveal pronounced anisotropic effects. Optical transmission studies show that nanostructured films, particularly those with pillar morphologies, display superior thermochromic performance, with increased transmission, enhanced infrared modulation, and broader hysteresis compared to dense films. The influence of nanostructure porosity on the optical response is also confirmed through simulations using both COMSOL and the Berreman matrix methods, which demonstrate strong agreement in reflectivity predictions. Our work represents a significant advancement in the synthesis of well-defined VO_2 nanostructures, opening new pathways for optimizing the material properties for advanced optical and thermochromic applications.

Keywords: keyword Vanadium dioxide, Thermochromism, Thin films, Glancing angle deposition, Mueller matrix ellipsometry, Optical simulation, COMSOL

1. Introduction

Vanadium dioxide (VO_2) is a well-known material with exceptional thermochromic properties, exhibiting a reversible phase transition around 68 °C [1]. This transition, which sees the material change from an insulating monoclinic to a metallic tetragonal state, is accompanied by a significant change in its optical and electrical properties. Because of this behavior, VO_2 is widely studied for applications in photonic devices [2], tunable optical filters [3, 4], and energy-saving windows [5, 6]. Research in this area has demonstrated that the thermochromic properties of VO_2 can be tuned by a variety of techniques, including chemical doping and mechanical stress.

Magnetron sputtering is a widely used deposition method for the synthesis of VO_2 thin films. This process allows precise control of film thickness and chemical composition, crucial elements for optimizing their thermochromic properties. However, to induce anisotropy on the VO_2 thin film, it is necessary to shape the film morphology with nanoscale precision. Glancing Angle Deposition (GLAD) technique is ideal for this purpose. By controlling the angle of incidence of the particle flux during deposition, GLAD method can be used to produce a variety of nanostructures, such as tilted columns patterns, or vertical pillars. These structures, because of their unique geometry, significantly influence the optical and electrical properties of materials, paving the way for advanced VO_2 functionalities. Many optical applications, such as broadband anti-reflection coatings [7], Bragg reflectors [8], and light-emitting diodes [9], depend on tailored effective optical constants achieved by controlling the porosity and morphology of nanostructured films. The nanostructured films obtained by GLAD are particularly useful for applications in sensors and optical devices, thanks to their large specific surface area and their ability to modulate optical [10–14] and electrical [15–19] properties.

However, this technique for synthesizing VO_2 films presents a number of difficulties, particularly in terms of the structural stability and the chemical composition. Y. Sun et al. investigated an alternative technique in which they attempted to reduce nanostructured V_2O_5 by annealing in a hydrogen environment in order to create monoclinic VO_2 nanostructures. While the production of nanostructures was successfully achieved with this approach, the annealing resulted in the coalescence of neighboring columns, making the columnar structure non-visible [20]. A.J. Santos et al. observed similar results after studying vanadium nanostructures during quick annealing in ambient air. Here again, column coalescence was observed [21]. To our knowledge, annealing a vanadium thin film in an oxygen environment has only been used in one study by A.M. Alcaide et al. [22] Unfortunately, results indicated that the film began to coalesce and the nanostructures were poorly defined. Furthermore, many other oxidation states were detected by Raman spectoscopy, suggesting that the film is still mainly composed of oxidation phases other than monoclinic VO_2. As a result, the film exhibits insufficient metal-insulator transition behavior on temperature-dependent transmission spectra.

The study of the optical properties of nanostructured materials, such as those obtained by GLAD, requires advanced analytical tools. Spectroscopic ellipsometry, and in particular the Mueller formalism, is a powerful method for characterizing these complex structures [23]. The Mueller formalism permits a complete description of the polarization state of light reflected from a material, giving detailed information on the optical anisotropy and birefringent properties of nanostructures. In the context of the analysis of nanostructured VO_2 films, this approach offers a better understanding of light-matter interactions within these systems, which is essential for optimizing their performance for specific applications.

2. Materials and Methods

2.1. Monoclinic VO_2 deposition

Reactive DC (direct-current) magnetron sputtering with low pressure plasma was employed for the deposition process. A 2 in diameter and 0.25 in thick target made of metallic vanadium with a purity of 99.99% was utilized. A turbomolecular pump driven by a dry main pump reached a residual pressure of $1.33\text{x}10^{-6}$ Pa before deposition. The target-to-substrate distance was 9 cm and the magnetron cathode was placed above the substrate holder. Substrates have a size of $\simeq 2 \times 2$ cm^2. A mixture of oxygen and argon was added to the chamber at a constant working pressure of 1 mTorr (0.13 Pa). The argon flux was held constant at 8 standard cubic centimeters per minute (sccm) during the deposition. A constant discharge current of 0.3 A was applied in order to deposit the vanadium oxide layer. The VO_2 monoclinic phase was produced by annealing the sample in a pure oxygen environment (about 400 Pa) within the same chamber after deposition. This process induced film crystallization and oxidation. (100) crystal silicon wafers, or BK7, constitute the substrate.

2.2. Characterization tools

High magnification pictures of the materials were obtained using a field emission gun scanning electron microscope (FEG-SEM Hitachi SU8020) using a 5 kV acceleration voltage. Grazing incidence X-ray diffraction (GIXRD) study was performed by using a Panalytical Empyrean with a Cu Kα source at 1.5406 Å to identify the crystalline structure. The X-ray beam's angle of incidence was kept constant at 1° with respect to the surface of the sample holder. Grain size is calculated using the Scherrer equation $D = (0.9\lambda)/(\alpha \cos\theta)$, where θ is the Bragg diffraction angle, λ the X-ray wavelength, α the line broadening at half the maximum intensity (FWHM) in radians, and D the mean size of the crystalline domains. A Bruker Senterra spectrometer equipped with a CCD detector and a HeNe laser (532 nm) generating at 20 mW was employed to perform Raman spectroscopy analysis. A Cary 5000 UV-Vis-NIR spectrometer was used to acquire transmission spectra in the 200–2500 nm range. Additionally, using a PerkinElmer Lambda 900 UV/Vis/NIR spectrometer, transmission spectroscopy was used to analyze the behavior of the optical transmittance of films deposited on glass. For transmission spectra, the temperature is set up to 25 °C and 100 °C thanks to a metal ceramic heater HT19R from Thorlabs with 4 mm-diameter holes to let the light pass through. This heater is connected to a power supply allowing to fix the temperature at 25 °C and 100 °C, respectively. In contrast, for the hysteresis measurement, a temperature range of 1 °C/min is managed with the THMS600 Linkam heating/cooling stage. Using a Horiba phase modulated UVISEL ellipsometer, the optical responses of thin films were investigated in the 0.6–4.76 eV spectral region at angles of incidence of 70°. Here again, a THMS600 Linkam stage is used to control the temperature at 25°C and 100°C.

2.3. Simulation tools

We used COMSOL Multiphysics to simulate electromagnetic fields and calculate reflection and transmission spectra. Our nanostructures are arranged in an infinite square lattice. To model this, we applied Floquet periodic boundary conditions to the left and right sides of the domain. A Port boundary condition at the top launches a plane wave at a specified incidence angle and computes the reflected light, while another at the bottom calculates the transmitted light. The electric field within each tetrahedral mesh element is approximated using a quadratic shape function. We employed 5 mesh elements per wavelength, and the refractive indices of VO_2 were determined via ellipsometry, as described in the previous section.

3. Dense and nanostructured VO_2 synthesis and characterization

In this section, we explore the synthesis of thermochromic VO_2 thin films, both dense and nanostructured, exhibiting open porosities. The substrate holder allows for two types of rotational movements: tilting the substrate from 0° to 90° relative to the cathode axis along the α tilt angle and continuously rotating the substrate with a speed ϕ_s. Depositing films with α angle superior to 80 ° creates a significant shadowing effect behind the initial nuclei of atoms and is the so-called GLAD (Glancing Angle Deposition) configuration. The shadowing results in thin film deposition where certain regions are inaccessible to the incoming atomic flux, leading to a highly porous structure. In the case of dense film, the substrate is parallel to the target plane and no rotation speed is used.

In this study, a specific angle $\alpha < 87$ was chosen accordingly and owing to previously reported data in the literature related to Glancing Angle Deposition of films, including our own works [15–22, 24, 25]. Various azimuthal substrate rotation speeds ϕ_s were employed: 0 and 1°/s. Knowing that monoclinic VO_2 is highly sensitive to oxidation, the porosity within the layer complicates the deposition process further. Consequently, deposition parameters such as oxygen flux and annealing duration had to be adjusted according to the desired morphology. Table 1 summarizes the deposition parameters used to develop both dense and structured monoclinic VO_2 films. The deposition time is calibrated to achieve a thickness of 200 nm. Our findings indicate that producing monoclinic VO_2 with higher porosity requires lower oxygen flux and shorter annealing times to achieve the same composition as a dense film. The increased porosity facilitates oxidation, thereby reducing the amount of oxygen needed to obtain comparable results.

Table 1: Deposition process parameters to synthesize a 200 nm-thick dense or nanostructured monoclinic VO_2.

	Dense	**Tilted**	**Pillar**
Rotation speed ϕ_s [°/s]	/	0	1
Angle of deposition α [°]	0	87	87
Deposition oxygen flux [sccm]	1.2	1	0.7
Annealing duration [min]	45	30	30
Annealing temperature [°C]	500	500	500
Deposition time [min]	13	60	30

The Raman spectra and GIXRD diffractogram for a dense and nanostructured thin film are displayed in Figures 1. The film shows 139, 193, 224, 264, 307, 389, 499, 613, and 825 cm^{-1} as monoclinic VO_2 vibration modes. At 973 cm^{-1}, a single peak that corresponds to V_7O_{16} emerges. The crystalline phase of our 1.2 sccm is next evaluated using GIXRD (Figure 1 b). It is apparent that there are no other oxidation states present, which is consistent with the findings of Raman analysis. In addition, the film looks strongly orientated with different crystalline orientation. The crystalline size, determined by using the Scherrer equation on

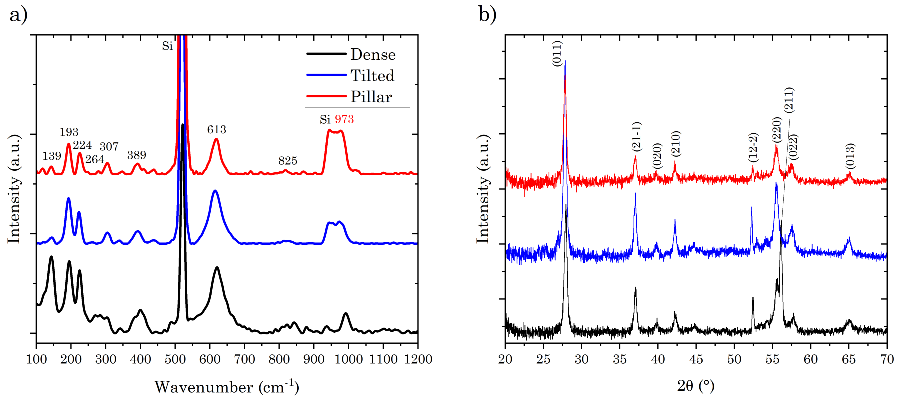

Figure 1: Raman spectra (a) and GIXRD diffractograms (b) of the 200 nm vanadium oxide thin films as measured at room temperature. Black and red label on Raman spectra refer to monoclinic VO_2 [26] and triclinic V_7O_{16} [27], respectively. GIXRD diffracted signals correspond to the monoclinic VO_2 phase, coming from JCPD 00-009-0142 card and [28]. Si notation concerns the silicon substrate signal.

three peaks, equals 20.1 ± 1.7 nm. Moreover, the chemical composition and crystalline structure of dense and nanostructured films are almost identical. Nevertheless, a difference is observed in the second Si peak at 950 cm^{-1}, which appears in nanostructured films due to their porosity.

Figure 2 focuses on the (011) diffraction peak, revealing a shift due to the presence of tensile strain in the nanostructured films compared to the dense films. With a uniform strain, the spacing of diffracted planes becomes larger and the diffraction peak shifts to the lower angles [29]. Additionally, the crystalline grain size decreases with increasing rotation speed, from 20.1 nm for dense VO_2 to 18.6 nm and 18.9 nm for tilted and pillar structures, respectively.

SEM images for dense and nanostructured VO_2 film are presented in Figure 3. In the same Figure, the morphologies are studied in terms of the column width

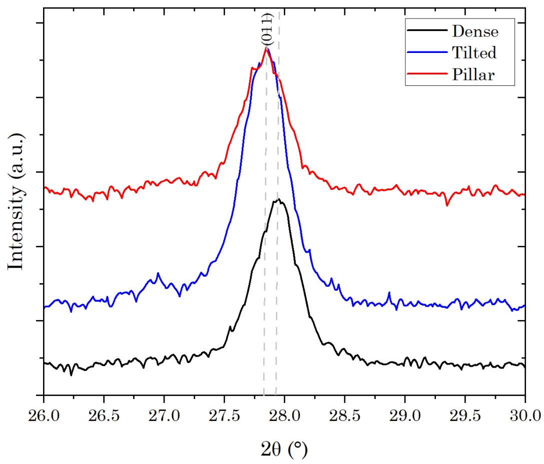

Figure 2: Shift of (011) monoclinic VO_2 X-ray diffraction peak for different film morphologies.

and the inter-columnar space. For dense film, the result shows a polycrystalline structure with grain-like surface topography typical of thin films grown by magnetron sputter deposition processes [30–32]. The structure of the films is greatly influenced by the deposition angle α and the rotation speed ϕ_s. Without rotation and with α = 87°, tilted columns (referred to as ”tilted”) are produced. The straight pillars are well defined at 1°/s (referred to as ”pillar”), although in that case, the pillar width increases along the film height. This phenomenon is also present with TiO_2 [24] and Al_2O_3 [25] GLAD films. Tilted columns have a spacing of around 105 nm, with a variation between 80 and 120 nm. Pillar-shaped columns, on the other hand, have a slightly smaller spacing of around 90 nm, with a range between 75 and 100 nm. Concerning the column width, inclined columns have a width of around 55 nm, with a result fluctuating between 45 and 65 nm. Pillar-shaped columns are wider, with a dimension of around 65 nm and an uncertainty that ranges from 50 to 80 nm. In summary, inclined columns show greater intercolumn spacing than pillar-shaped columns, while the latter are wider.

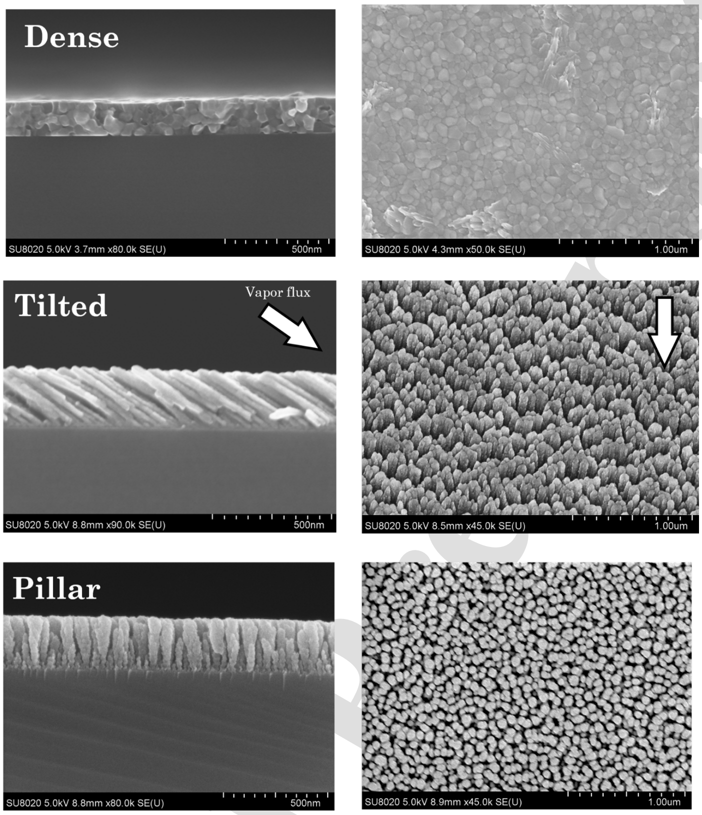

Figure 3: Cross-sectional and top-view SEM images of monoclinic VO_2 deposited according to the Table 1 parameters. All images are obtained for film directly after the annealing procedure. The arrow represents the direction of the incoming vapor flux.

Figures 1 and 3 illustrate that our synthesis procedure, utilizing 0.7 sccm of O_2 and post-deposition annealing at 500 °C for 30 minutes, successfully produces well-defined nanostructures of pure monoclinic VO_2.

Our nanostructured films were characterized in terms of their optical properties. Figure 4 presents transmission spectra and hysteresis for dense and nanostructured films at 25 °C and 100 °C. This demonstrates that the gaps between the cold and hot state spectra are significantly enhanced when the films are structured at the nanoscale. At a wavelength of 2500 nm (Figure 4b), the transmission variation for dense film is around 20%. The value is improved for pillar and tilted films, with gaps of 37.2%, and 47.9%, respectively. Additionally, pillar morphology results in a 10% increase in visible transmission compared to tilted, resulting in no change in transmission. Based on the VO_2 phase change, we presume that these improvements are caused by the larger porosity of the nanostructured films. This will enhance light sensitivity and boost light transmission through the layer.

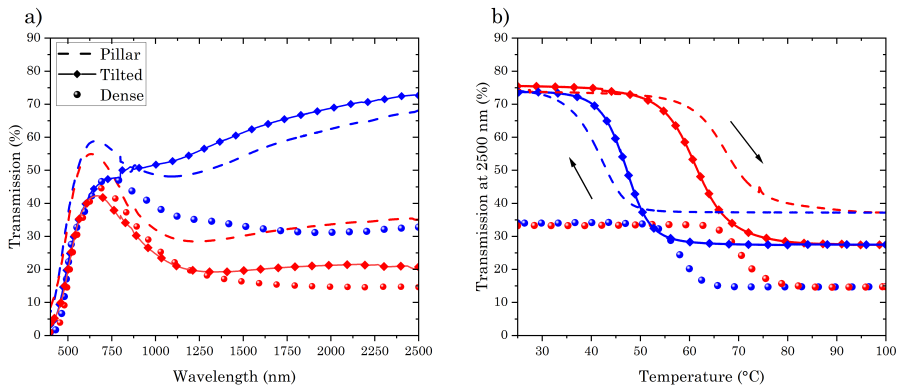

Figure 4: Experimental transmission spectra (a) and hysteresis loops (b) at 2500 nm for dense, tilted and straight pillars at 25 °C (blue) and 100 °C (red).

To further emphasize the insulator to metal transition of the deposited VO_2 films, in-plane resistivity measurements were carried out. Data are reported in Fig. 5 and evidence the variation of the electrical properties of the deposited "dense" and "tilted" films as a function of the temperature. The pillar nanostructure is not shown because the measurement failed to give results due to technical limitations. As the film resistivity is too high, the current source and ampere meter are not sensitive enough for accurate measurements.

The hysteresis characteristics of dense and nanostructured VO_2 films are com-

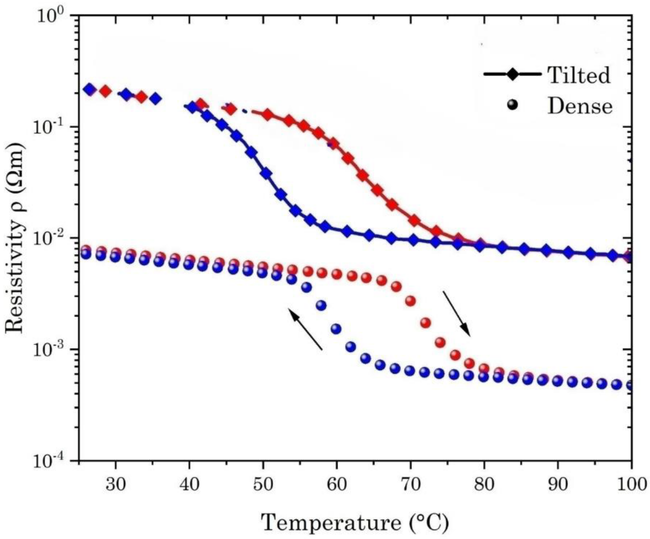

Figure 5: Resistivity hysteresis loops for the dense films (filled circles) and the tilted pillars (filled losange).

pared in Table 2. The critical temperature during the heating and cooling ramp, the transition amplitude, and the hysteresis width are the reported parameters. The values representing the critical temperature are obtained at the middle point of the total amplitude. Compared to dense films, nanostructured films exhibit larger hysteresis widths and lower average critical temperatures. This phenomenon is potentially due to the stress observable in nanostructured thin films in Figure 2. The relationship between stress and changes in the hysteresis width and critical temperature is documented in recent research [33–35]. Furthermore, a considerable rise in hysteresis width, indicating a delayed phase transition, is seen for the films made of straight pillars suggesting that an increase in inter-column spacing (see Fig. 3 for film morphologies) might play a role in this effect. It is hypothesized that an increase in porosity will delay the "hot" phase propagation throughout the layer. Finally, films having a higher volume proportion of VO_2 in the layer, tend to have stronger light attenuation.

Table 2: Hysteresis parameters of the dense and nanostructured films, deposited with different rotation speeds ϕ_s.

ϕ_s (°/s)	**Critical Temperature (°C)**			**Width (°C)**	**Amplitude (%)**
	Heating	Cooling	Average		
/ (Dense)	70	57.4	63.7	12.6	18.4
0 (Tilted)	61.3	47.2	54.2	14.1	47.9
1 (Pillar)	67.7	41.1	54.4	26.6	37.2

4. Ellipsometric study of dense and tilted structures

In this section, ellipsometric measurements of I_s and I_c intensities (defined in supporting information in Eq. 1 in *Supporting information*) have been carried out for both metallic and insulating VO_2 states as a function of wavelength in order to determine the dielectric functions of dense, tilted films. Concerning the dense film, two measurements are performed with different angles of incidence (AOI) at 60 ° and 70 °. The experimental and modeled data from the fitting model are shown by the continuous and dotted lines, respectively, in Figure SI-1 in *Supporting information*, demonstrating a good match between experiment and model. For the latter, the sample is represented as a three-layer film composed of a rough top layer, a dense VO_2 layer and a semi-infinite silicon substrate, with air as ambient material (Figure 6a). The surface roughness is mandatory because ellipsometry measurements are highly sensitive to the surface characteristics. This layer is

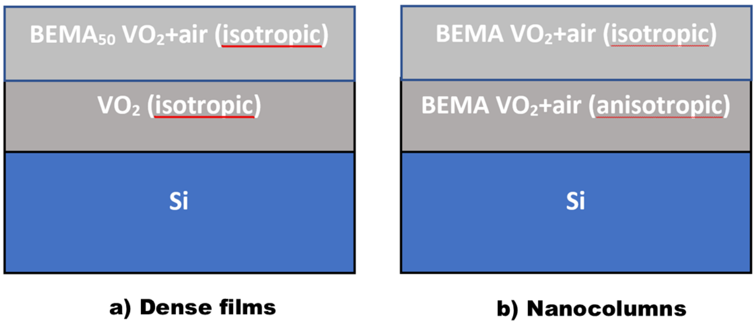

Figure 6: Ellipsometric model for a) the dense films and b) the tilted nanocolums.

modeled by a Bruggeman effective medium approximation with a 50%:50% mixture of VO_2 and air ($BEMA_{50}$) given by

$$\frac{\epsilon_{VO_2} - \epsilon_{eff}}{\epsilon_{VO_2} + 2\epsilon_{eff}} + \frac{1 - \epsilon_{eff}}{1 + 2\epsilon_{eff}} = 0 \quad (1)$$

where ϵ_{eff} is the effective dielectric function. At room temperature, the VO_2 dielectric function is modeled as a sum of three Lorentz oscillators, as explained hereafter, and a static dielectric term. A Drude term is added at 100 °C to model the metallic behavior.

Several authors used 3 Lorentzian oscillators to model the dispersion law VO_2 at room temperature [36–38]. According to calculation made with the Full-Potential Linear-Muffin-Tin Orbital Method [39], the Lorentz oscillators located at low-energy, mid-range and high-energy can be attributed to the $d-d$ transitions to unoccupied t_{2g} states, the $d-d$ transitions to the unoccupied $d_{||*}$ band and the $d-d$ transitions to unoccupied e_g states of VO_2.

The corresponding dielectric function for dense and tilted samples is plotted in Figure 7.

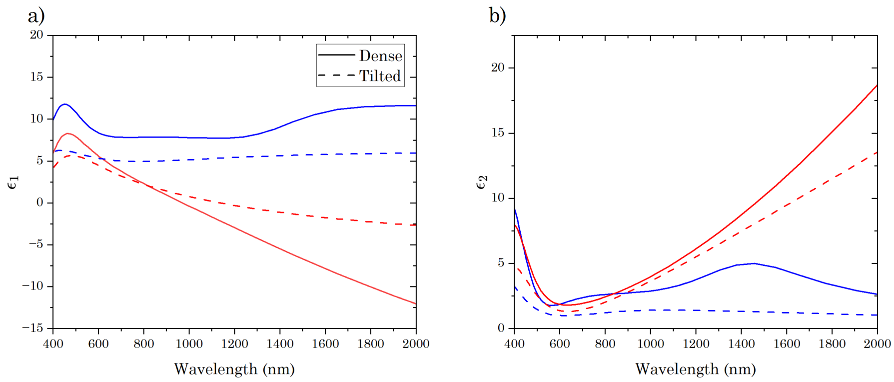

Figure 7: (a) Real ϵ_1 and (b) imaginary ϵ_2 part of permittivity part for dense, tilted films at 25 °C (blue) and 100 °C (red).

In the case of tilted columns, the measurements have been performed at two distinct sample azimuthal angles, 0 ° and 90 °. The angles 0 ° and 90 ° mean that the nanocolumns are parallel and perpendicular to the incidence plane, respectively. Here, the fitting model consists of two Bruggeman layers describing mixtures of air and VO_2. The first one is isotropic and corresponds to the roughness layer at the top of the sample. The second one is anisotropic with an uniaxial optical axis tilted at 55 ° with respect to the normal of incidence (i.e. with 35 ° with respect to the silicon substrate; angle calculated using Figure 3) to simulate columns (Figure 6b). For the roughness layer with a f_{VO_2} fraction, the effective dielectric function ϵ_{eff} is given by

$$f_{VO_2}\frac{\epsilon_{VO_2}-\epsilon_{eff}}{\epsilon_{VO_2}+2\epsilon_{eff}}+(1-f_{VO_2})\frac{1-\epsilon_{eff}}{1+2\epsilon_{eff}}=0 \tag{2}$$

For the anisotropic layer, characterized by a effective dielectric tensor and a f_{VO_2} fraction, the effective medium approximations for the ordinary $\epsilon_{eff,o}$ dielectric function is given by the same equation as Eq. 2 (with a different volume fraction) while the extraordinary $\epsilon_{eff,e}$ dielectric function is

$$\epsilon_{eff,e} = f_{VO_2}\epsilon_{VO_2} + (1 - f_{VO_2}) \quad (3)$$

The model has been adjusted based on the VO_2 volume fraction of the anisotropic and the roughness layer, but also on the intrinsic dielectric function of VO_2 itself. The VO_2 volume fraction given by the model is 84% and 54% for the anisotropic layer and the roughness, respectively. The experimental and simulated results are presented in Figure SI-2 in *Supporting information*.

A Mueller matrix ellipsometer can be used to study the structural anisotropy of ”tilted” samples. To do this, the light angle of incidence and the wavelength are fixed at 70 ° and 470 nm, respectively. Concerning the tilted nanocolumns, the measurement of the Mueller matrix in Figure 8 is performed according to the sample azimuth rotation at each step of 10 °. The most comprehensive kind of ellipsometry measurement is the Mueller matrix ellipsometry, which may be used to access cross-polarization optical signals. As explained before, generalized ellipsometry analysis characterizes samples where cross-polarization is present. With a more general definition, cross-polarization is defined by a light-sample interaction that results in a mixed-polarization state response when the incoming light is totally polarized (linearly or circularly). A description of the Mueller matrix elements is provided in the supporting information.

The starting value, when azimuth = 0 °, is configured for tilted nanocolumns oriented in the direction of the incoming light and parallel to the incidence plane. It is important to note that the last columns of the matrix composed of M_{14}, M_{24}, M_{34}, and M_{44} are not measured because we work with an ellipsometer configuration where a photoelastic modulator is placed after the sample. The tilted sample is the only one that was analyzed according to the sample azimuth angle because, in view of its morphology, it is expected to show an optical signal largely influenced by sample orientation. In contrast to helices and pillars, where the orientation of nanostructures will be less responsive to rotation.

Firstly, we clearly see that the azimuth angle has a strong influence on the Mueller matrix elements. In addition, the off-diagonal 2x2 block data (M_{31}, M_{32}, M_{41}, M_{42}, M_{13} and M_{23}) equal 0 and M_{22} equals 1 for azimuth 0 ° and 180 °, which coincide with the orientations of the sample when the tilted columns are parallel to the plane of incidence. At this special orientation, the sample is considered as pseudo-isotropic, where no p-polarization light is converted into s-polarized light and vice versa [23]. At this orientation, the Mueller matrix is similar to the one expressed for isotropic samples. We also remark that the off-diagonal blocks are not, or slightly, impacted by heating compared to other elements.

Secondly, we can interpret all elements of the Mueller matrix [40]. For example, the first row is interpreted as the diattenuation elements. About vertical and horizontal polarization, negative M_{12} means that the total reflected intensity is higher when the incident light is polarized vertically compared to horizontally. Nevertheless, $M_{12} \neq -1$, so the sample also interacts with horizontal polarization. For M_{13} it is more complicated, because the values are negative before 180 ° of sample rotation, and positive after 180 °. This means that the reflected light intensity is maximized when the incoming light is polarized at -45 ° or +45 °, depending on whether the column orientation is 90 ° or 270 °, respectively. We suppose that this is because the sample is composed of tilted nanocolumns, and at a specific orientation, the columns are parallel or perpendicular to the polarization direction. With a polarization of +45 °, the columns are parallel to the light direction when the sample is rotated by 90 °. On the other hand, the columns are perpendicular to the light when the sample is rotated by 180 °. Note here that they are not exactly parallel and perpendicular because the nanocolumns are tilted by 55 ° and not 45 ° (Fig. 3).

By focusing on the first column of the matrix, the elements are now related to the polarizance effect. M_{21} presents the same behavior as M_{12}, but here, the interpretation says that when an unpolarized light is sent to the sample, the resulting light is mostly vertically polarized. In addition, M_{31} corresponds to the ability of the sample to polarize linearly at +45 ° (for positive values) or -45 ° (for negative values) when unpolarized light interacts with the sample. In our case, nanocolumns rotated by 90 ° transform unpolarized light into -45 ° linear polarization, and, in contrast, when they are rotated by 270 °, the final polarization is +45 ° linear. Regarding M_{31}, the interpretation is the same as except that now, unpolarized light becomes right circularly polarized by 90 ° of azimuthal rotation and left circularly polarized by 270 ° of rotation. Finally, M_{22} = 1 for a sample that is rotated by 0 ° and 180 °. The result means that at this orientation, horizontally and vertically polarized light stay in the same polarization state after reflection.

5. Optical characterization and simulation

In this section, the optical response of the nanostructured samples, both straight and tilted pillars, is rigorously calculated using finite-element simulations of the Maxwell equations by the software COMSOL Multiphysics.

The straight pillars are modeled as conical shapes, see Fig. 9(a), with a spherical top, according to the SEM image analysis (Fig. 3). The intercolumnar space is fixed at 10 nm, and the column width is 80 nm at the top and 25 nm at the bottom.

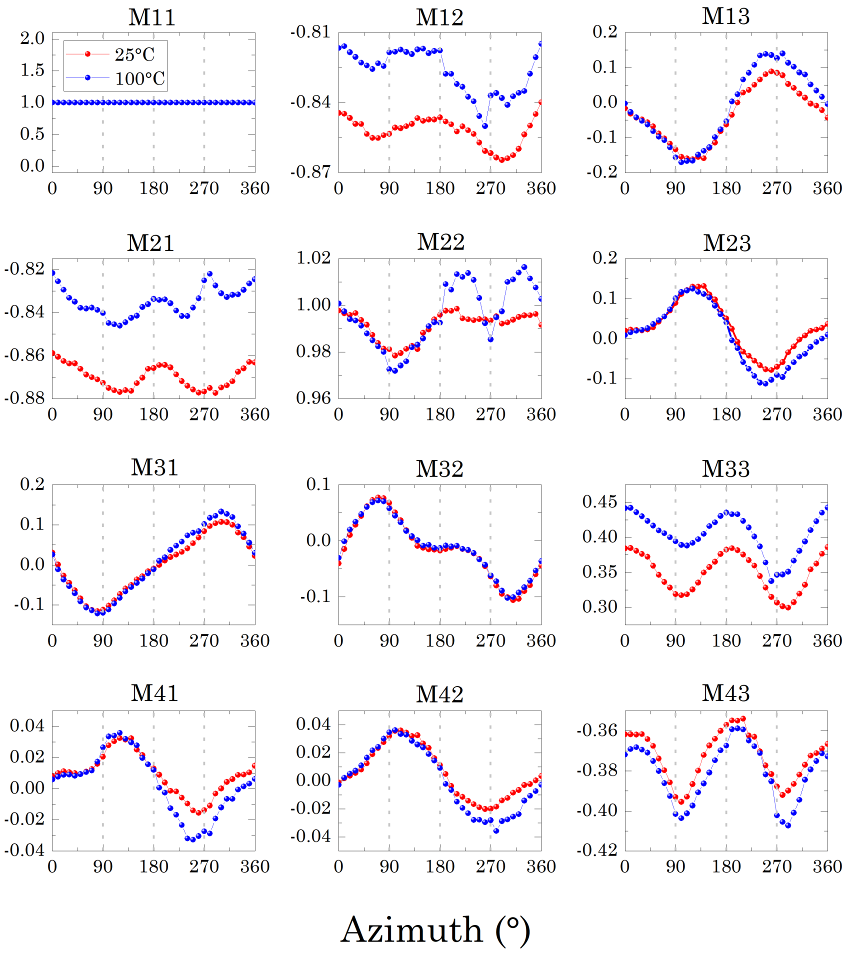

Figure 8: Experimental Mueller matrix data of a monoclinic VO_2 tilted columnar thin film versus sample azimuth angle at λ = 470 nm. The light incidence angle is fixed at 70 °. The temperature samples are 25 °C (blue) and 100 °C (red). Vertical lines are put at 90 °, 180 ° and 270 ° of azimuth. All elements are normalized by the M_{11} value.

The total height of the structure is 270 nm. The substrate is glass with a thin 5 nm VO_2 overlayer. The pillars are 3D, set in a 2D square lattice with period 90 nm.

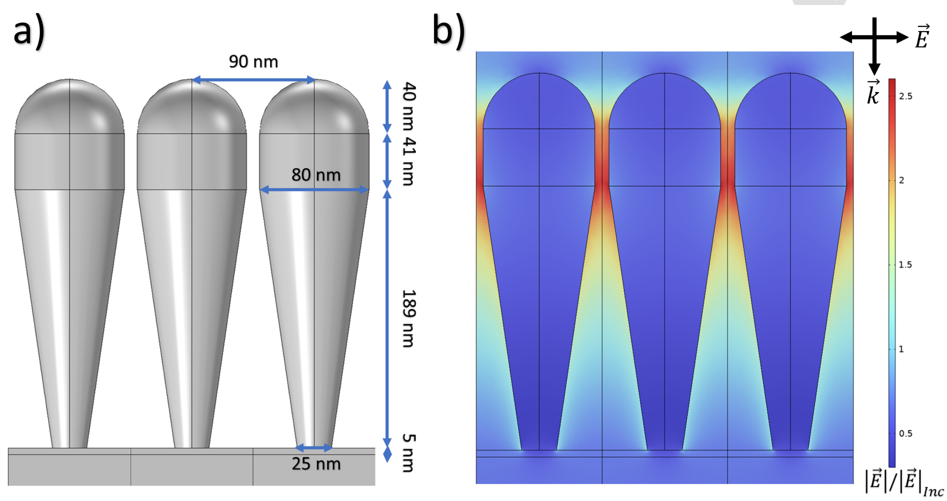

Figure 9: a) Simulation model. For visualization three periods are shown side by side, but only one period needs to be simulated. b) Plot of the electric field enhancement for pillars in the hot state at wavelength 700 nm.

For this model, a representative electrical field profile at wavelength 700 nm, for VO_2 in the hot state, is shown in Fig. 9(b). The arrow $\vec{E}$ indicates the polarization direction of the incident electric field, while $\vec{k}$ shows the perpendicular incidence. The color scale is normalized with respect to the incident amplitude, showing an interestingly strong light concentration in the narrow region between the straight cylinder sections. This behavior can be understood via the 'slot waveguide' effect, stemming from the perpendicular boundary condition for electric fields at an interface: $\epsilon_{VO_2} E_{n,VO_2} = \epsilon_{air} E_{n,air}$, with E_n the component normal to the interface. Since $\epsilon_{VO_2} > \epsilon_{air}$, there is a higher normal electric field component just outside the two nearby interfaces, leading to notable field concentration.

The transmission spectra for cold and hot VO_2 were simulated, see Figure 10.

For this structure, the cold transmission (blue) is around 57% at a wavelength of 500 nm. This curve nearly continuously increases, leveling off beyond 1500 nm, reaching about 90 % near 2000 nm. By comparing with Figure 4a (dashed blue and red curves), the pillar follow a similar trend, starting around 30 % at 500 nm, rising to $\sim$ 50 % at 1000 nm, leveling off to $\sim$ 70 % at 2500 nm.

The simulations obtain higher transmission (90 % at 2000 nm) compared to experiment, mainly at higher wavelengths. A potential, but probably limited, difference is the refractive index used in the simulation, which is the one measured for a sample on silicon (for ellipsometry measurements), and not for the sample on glass (for transmission measurements). However, previous research [41] shows only marginal variations in VO_2 refractive indices between silicon and glass substrates. A more important difference factor is the arrangement of the nanostructures on the substrate. In the simulations, the nanostructures are modeled in a perfectly ordered lattice, whereas in the experiment the nanostructures are quite randomly distributed on the substrate, which influences the transmission. It turns out that for simulations a major factor is the filling factor of the pillars (width of pillars versus period), whereas the precise shape (e.g., conical radius) is of lesser importance.

Next, Figure 11a illustrates the geometry of the model to simulate the optical properties of slanted VO_2 nanocolumns. The setup consists of nanocolumns composed of a rod radius of 32.5 nm and a spherical top, inclined at an angle to the silicon substrate of 35 °. The nanocolums are 3D, set in a 2D square lattice with period (intercolumn distance) 64.5 nm. Since this distance is less than twice the radius of the columns, they exhibit an overlap in both the x (horizontal) and y (in-plane) directions. This choice was motivated by the analysis of the SEM

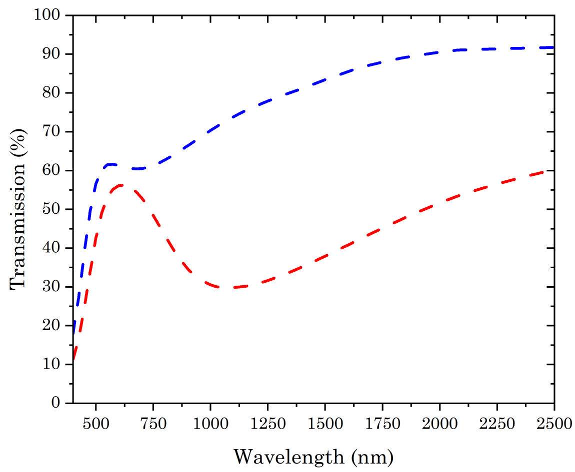

Figure 10: Simulated transmission spectra in cold (blue) and hot (red) state of straight pillar morphology represented in Figure 9.

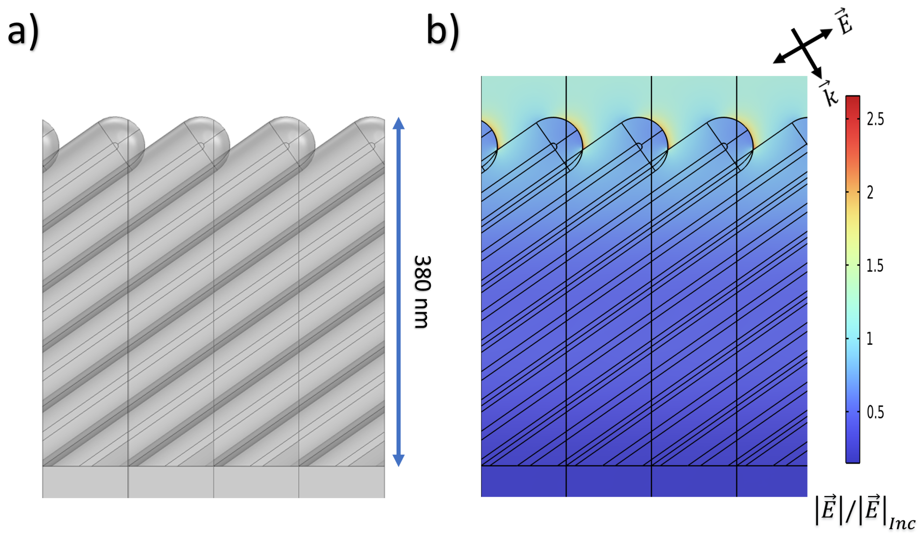

Figure 11: a) Simulation model of tilted nanocolumn morphology. For visualization four periods are shown side by side, but only one period needs to be simulated. b) Plot of the electric field enhancement for tilted nanocolumns in the hot state at wavelength 700 nm.

images (Fig. 3), which are quite dense. Note that there are still important air pores between the pillars. This setup thus allows for the investigation of reflectivity and transmittance by modeling the structure's anisotropic response to incident light.

The field plot in Fig. 11 (b) displays the electrical field profile, at wavelength 700 nm, within this tilted nanocolumn morphology when VO_2 is in the hot state. The area of electric field enhancement on the spherical top can also be explained by the discontinuity of the electric field perpendicular to the interface, as already noticed for the straight nanopillars.

We examine and compare the reflectivity with two distinct simulation techniques, Figure 12 shows results obtained using COMSOL (orange curves) and a Berreman 4x4 matrix transfer method (green curves) at incident angles of 0°, 30°, and 60°. The left and right columns represent the cold and hot states of VO_2, respectively.

In the COMSOL simulation approach, the slanted nanocolumn structure is modeled three-dimensionally, capturing the precise shape, orientation, and arrangement of individual nanocolumns, which provides a detailed representation of the *porous*, nanostructured surface. In contrast, the Berreman 4x4 matrix transfer method models the nanocolumn system as an *anisotropic* bulk material with a tilted optical axis. This technique simplifies the structure by treating the material as a layered medium with an inclined optical axis, thus accounting for the overall anisotropy without explicitly simulating each column. The Berreman method calculates a transfer matrix for each layer, which encapsulates how light is reflected and transmitted within that layer, allowing for the derivation of the overall optical response of the material across multiple layers.

Both methods demonstrate strong agreement in the reflectivity results. Despite

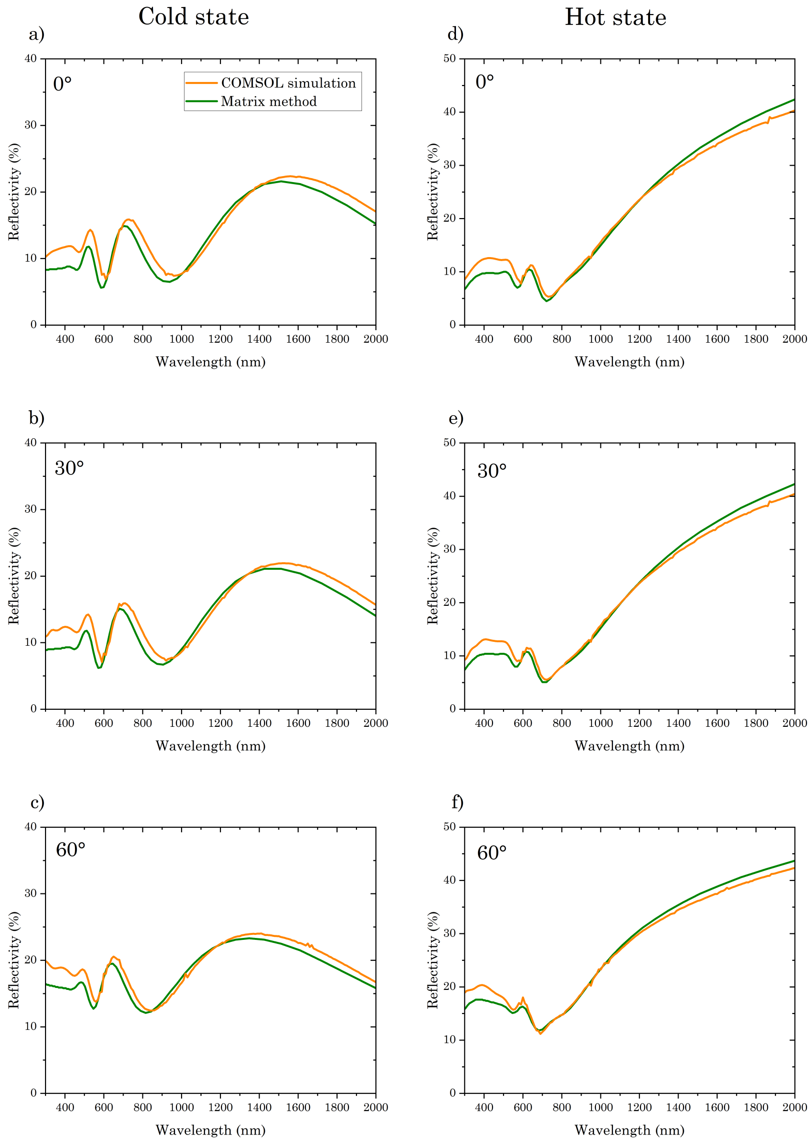

Figure 12: Reflectivity simulation for tilted nanocolumns using COMSOL (orange lines) and the Berreman matrix technique (green lines) at 0°, 30° and 60° of angle of incidence. The left and right columns represents the cold and hot states, respectively.

the modeling differences—where COMSOL provides detailed 3D simulation and Berreman simplifies the system as a bulk material—the reflectivity spectra at various angles of incidence (0°, 30°, and 60°) and in both thermal states of VO_2 align closely. This comparison illustrates that the Berreman matrix transfer method offers a practical, less complex alternative to COMSOL for simulating optical properties of this slanted nanocolumn systems, while still yielding comparable results.

6. Conclusion

This study demonstrates the significant impact of nanostructure morphology on the optical and thermochromic properties of monoclinic vanadium dioxide thin films. By utilizing the Glancing Angle Deposition (GLAD) technique, we successfully synthesized anisotropic VO_2 nanostructures, including tilted and pillar-like morphologies, which markedly enhance the thermochromic performance of the films.

In particular, the pillar morphology exhibits larger transmission variation and broader hysteresis, making them especially promising for applications requiring tunable optical properties such as energy-efficient smart windows. Optical characterization using azimuthal Mueller matrix measurements reveal a strong correlation between nanostructure geometry and optical anisotropy, with the tilted nanocolumns showing pronounced polarization effects depending on the sample's rotation.

Finite element simulations and modeling approaches such as the Berreman 4x4 transfer matrix method provide valuable insights into the behavior of these nanostructures. The results highlight the critical role that the porosity of VO_2

plays in its optical response, suggesting new opportunities for optimizing these materials in photonic devices, sensors and tunable optical filters. Overall, our findings significantly advance the understanding of VO_2 nanostructures and open new ways for their application in cutting-edge optical technologies.

CrediT authorship contribution statement

G. Savorianakis: Investigation, Formal analysis, Writing - original draft. C. Rousseau: Investigation, Formal analysis, Writing - original draft. A. En Naciri: Writing – review & editing, Conceptualization. Y. Battie: Investigation, Formal analysis, Conceptualization, Writing – review & editing. B. Maes: Supervision, Conceptualization, Writing – review & editing. M. Voué: Supervision, Conceptualization, Writing – review & editing. S. Konstantinidis: Supervision, Conceptualization, Writing – review & editing.

Declaration of competing interest

The authors declare that they have no known competing financial interests or personal relationships that could have appeared to influence the work reported in this paper.

Data availability

Experimental and simulation data are available upon request to the corresponding author.

Acknowledgments

This work was supported by the Fonds de la Recherche Scientifique - FNRS under Grant n° 40003517. S.K. is Research Director of the FNRS and G.S. acknowledges the FNRS for financial support through the FRIA grant n° 40004184. C.R. and B.M. acknowledge support from the Action de Recherche Concertée (project ARC-23/27 UMONS3).

Appendix A. Supporting information

Supporting information to this article can be found online at ...

References

[1] F. J. Morin, Oxides which show a metal-to-insulator transition at the neel temperature, Physical Review Letters 3 (1959) 34–36. doi:10.1103/PhysRevLett.3.34.

[2] G. Savorianakis, K. Mita, T. Shimizu, S. Konstantinidis, M. Voué, B. Maes, VO_2 nanostripe-based thin film with optimized color and solar characteristics for smart windows, Journal of Applied Physics 129 (2021) 185306. doi:10.1063/5.0049284.

[3] M. A. Kats, D. Sharma, J. Lin, P. Genevet, R. Blanchard, Z. Yang, M. M. Qazilbash, D. N. Basov, S. Ramanathan, F. Capasso, Ultra-thin perfect absorber employing a tunable phase change material, Applied Physics Letters 101 (2012) 221101. doi:10.1063/1.4767646.

[4] G. Savorianakis, C. Rousseau, A. Sergievskaya, G. Rosolen, M. Voué, B. Maes, S. Konstantinidis, Plasmonic resonance shifts in gold

nanoparticles-thermochromic VO_2 thin film hybrid platforms: A joint experimental and numerical study, Advanced Materials Interfaces (2024) 2400172 doi:10.1002/admi.202400172.

[5] Y. Cui, Y. Ke, C. Liu, Z. Chen, N. Wang, L. Zhang, Y. Zhou, S. Wang, Y. Gao, Y. Long, Thermochromic VO_2 for energy-efficient smart windows, Joule 2 (2018) 1707–1746. doi:j.joule.2018.06.018.

[6] B. Li, S. Tian, L. Zhou, S. Wu, T. Ma, G. He, B. Liu, X. Zhao, Fully Discrete VO_2 Particulate Film with Ultra-High Transmittance and Excellent Thermochromic Performance, Advanced Optical Materials (2023) 2302042 doi:10.1002/adom.202302042.

[7] T. Tolenis, L. Grinevičiūtė, R. Buzelis, L. Smalakys, E. Pupka, S. Melnikas, A. Selskis, R. Drazdys, A. Melninkaitis, Sculptured anti-reflection coatings for high power lasers, Optical Materials Express 7 (2017) 1249–1258. doi:10.1364/OME.7.001249.

[8] J. W. Leem, J. S. Yu, Broadband and wide-angle distributed bragg reflectors based on amorphous germanium films by glancing angle deposition, Optics Express 20 (2012) 20576–20581. doi:10.1364/OE.20.020576.

[9] L. Lu, Z. Xu, F. Zhang, S. Zhao, L. Wang, Z. Zhuo, D. Song, H. Zhu, Y. Wang, Using ZnS nanostructured thin films to enhance light extraction from organic light-emitting diodes, Energy & Fuels 24 (2010) 3743–3747. doi:10.1021/ef901327c.

[10] T. Motohiro, Y. Taga, Thin film retardation plate by oblique deposition, Applied Optics 28 (1989) 2466–2482. doi:10.1364/AO.28.002466.

[11] S. R. Kennedy, M. J. Brett, Porous broadband antireflection coating by glancing angle deposition, Applied Optics 42 (2003) 4573–4579. doi:10.1364/AO.42.004573.

[12] J.-Q. Xi, M. F. Schubert, J. K. Kim, E. F. Schubert, M. Chen, S.-Y. Lin, W. Liu, J. A. Smart, Optical thin-film materials with low refractive index for broadband elimination of fresnel reflection, Nature Photonics 1 (2007) 176–179. doi:10.1038/nphoton.2007.26.

[13] M. O. Jensen, M. J. Brett, Square spiral 3d photonic bandgap crystals at telecommunications frequencies, Optics Express 13 (2005) 3348–3354. doi:10.1364/OPEX.13.003348.

[14] M. T. Tanvir, K. Fushimi, Y. Aoki, H. Habazaki, Oblique angle deposition of columnar niobium films for capacitor application, Materials Transactions 49 (2008) 1320–1326. doi:10.2320/matertrans.MRA2007313.

[15] M. Sampaio Rodrigues, P. Fiedler, N. Küchler, R. Domingues, C. Lopes, J. Borges, J. Haueisen, F. Vaz, Dry electrodes for surface electromyography based on architectured titanium thin films, Materials 13 (2020) 2135. doi:10.3390/ma13092135.

[16] A. Chargui, R. El Beainou, A. Mosset, S. Euphrasie, V. Potin, P. Vairac, N. Martin, Influence of thickness and sputtering pressure on electrical resistivity and elastic wave propagation in oriented columnar tungsten thin films, Nanomaterials 10 (2020) 81. doi:10.3390/nano10010081.

[17] R. El Beainou, J.-M. Cote, V. Tissot, V. Potin, N. Martin, Resistivity

anisotropy of tilted columnar W and WCu thin films, Surface and Coatings Technology 421 (2021) 127412. doi:10.1016/j.surfcoat.2021.127412.

[18] R. El Beainou, N. Martin, V. Potin, P. Pedrosa, M. A. P. Yazdi, A. Billard, Correlation between structure and electrical resistivity of W-Cu thin films prepared by GLAD co-sputtering, Surface and Coatings Technology 313 (2017) 1–7. doi:10.1016/j.surfcoat.2017.01.039.

[19] J. Potočnik, M. Nenadovic, B. Jokić, M. Popović, Z. Rakočević, Properties of zig-zag nickel nanostructures obtained by GLAD technique, Science of Sintering 48 (2016) 51. doi:10.2298/SOS1601051P.

[20] Y. Sun, X. Xiao, G. Xu, G. Dong, G. Chai, H. Zhang, P. Liu, H. Zhu, Y. Zhan, Anisotropic vanadium dioxide sculptured thin films with superior thermochromic properties, Scientific Reports 3 (2013) 2756. doi:10.1038/srep02756.

[21] A. J. Santos, B. Lacroix, M. Domínguez, R. García, N. Martin, F. M. Morales, Controlled grain-size thermochromic VO_2 coatings by the fast oxidation of sputtered vanadium or vanadium oxide films deposited at glancing angles, Surfaces and Interfaces 27 (2021) 101581. doi:10.1016/j.surfin.2021.101581.

[22] A. M. Alcaide, G. Regodon, F. J. Ferrer, V. Rico, R. Alvarez, T. C. Rojas, A. R. González-Elipe, A. Palmero, Low temperature nucleation of thermochromic VO_2 crystal domains in nanocolumnar porous thin films, Nanotechnology 34 (2023) 255702. doi:10.1088/1361-6528/acc664.

[23] O. Arteaga, Useful Mueller matrix symmetries for ellipsometry, Thin Solid Films 571 (2014) 584–588. doi:10.1016/j.tsf.2013.10.101.

[24] J. Dervaux, P. A. Cormier, P. Moskovkin, O. Douheret, S. Konstantinidis, R. Lazzaroni, S. Lucas, R. Snyders, Synthesis of nanostructured Ti thin films by combining glancing angle deposition and magnetron sputtering: A joint experimental and modeling study, Thin Solid Films 636 (2017) 644–657. doi:10.1016/j.tsf.2017.06.006.

[25] H.-H. Jeong, A. Mark, J. Gibbs, T. Reindl, U. Waizmann, J. Weis, P. Fischer, Shape control in wafer-based aperiodic 3D nanostructures, Nanotechnology 25 (2014) 235302. doi:10.1088/0957-4484/25/23/235302.

[26] F. Ureña-Begara, A. Crunteanu, J.-P. Raskin, Raman and XPS characterization of vanadium oxide thin films with temperature, Applied Surface Science 403 (2017) 717–727. doi:10.1016/j.apsusc.2017.01.160.

[27] J. Huotari, J. Lappalainen, J. Eriksson, R. Bjorklund, E. Heinonen, I. Miinalainen, J. Puustinen, A. Lloyd Spetz, Synthesis of nanostructured solid-state phases of V_7O_{16} and V_2O_5 compounds for ppb-level detection of ammonia, Journal of Alloys and Compounds 675 (2016) 433–440. doi:10.1016/j.jallcom.2016.03.116.

[28] K. D. Rogers, An x-ray diffraction study of semiconductor and metallic vanadium dioxide, Powder Diffraction 8 (1993) 240–244. doi:10.1017/S0885715600019448.

[29] B. Nasiri-Tabrizi, Thermal treatment effect on structural features of mechano-synthesized fluorapatite-titania nanocomposite: A comparative

study, Journal of Advanced Ceramics 3 (2014) 31–42. doi:10.1007/s40145-014-0090-4.

[30] M. Tangirala, K. Zhang, D. Nminibapiel, V. Pallem, C. Dussarrat, W. Cao, T. Adam, C. Johnson, H. Elsayed-Ali, H. Baumgart, Physical analysis of VO_2 films grown by atomic layer deposition and RF magnetron sputtering, ECS Journal of Solid State Science and Technology 3 (2014) N89–N94. doi:10.1149/2.006406jss.

[31] C. Zhang, C. Koughia, O. Güneş, J. Luo, N. Hossain, Y. Li, X. Cui, S.-J. Wen, R. Wong, Q. Yang, S. Kasap, Synthesis, structure and optical properties of high-quality VO_2 thin films grown on silicon, quartz and sapphire substrates by high temperature magnetron sputtering: Properties through the transition temperature, Journal of Alloys and Compounds 848 (2020) 156323. doi:10.1016/j.jallcom.2020.156323.

[32] J. A. Thornton, The microstructure of sputter-deposited coatings, Journal of Vacuum Science & Technology A 4 (1986) 3059–3065. doi:10.1116/1.573628.

[33] E. Gagaoudakis, E. Verveniotis, Y. Okawa, G. Michail, E. Aperathitis, E. Mantsiou, G. Kiriakidis, V. Binas, Study on the surface morphology of thermochromic rf-sputtered VO_2 films using temperature-dependent atomic force microscopy, Applied Sciences 13 (2023) 7662. doi:10.3390/app13137662.

[34] D. H. Jung, H. S. So, K. Ko, J.-W. Park, H. Lee, T. Nguyen, S. Yoon, Electrical and optical properties of VO_2 thin films grown on various sapphire

substrates by using RF sputtering deposition, Journal of the Korean Physical Society 69 (2016) 1787–1797. doi:10.3938/jkps.69.1787.

[35] J. Bian, M. Wang, H. Sun, H. Liu, X. Li, Y. Luo, Y. Zhang, Thickness-modulated metal–insulator transition of VO_2 film grown on sapphire substrate by MBE, Journal of Materials Science 51 (2016).

[36] P. Ashok, Y. Chauhan, A. Verma, High infrared reflectance modulation in VO_2 films synthesized on glass and ITO coated glass substrates using atmospheric oxidation of vanadium, Optical Materials 110 (2020) 110438. doi:10.1016/j.optmat.2020.110438.

[37] Y. Guo, Y. Zhang, X. Chai, L. Zhang, L. Wu, Y. Cao, L. Song, Tunable broadband, wide angle and lithography-free absorber in the near-infrared using an ultrathin VO_2 film, Applied Physics Express 12 (2019) 071005. doi:10.7567/1882-0786/ab29e4.

[38] K. Dai, J. Lian, M. J. Miller, J. Wang, Y. Shi, Y. Liu, H. Song, X. Wang, Optical properties of VO_2 thin films deposited on different glass substrates, Opt. Mater. Express 9 (2019) 663–672. doi:10.1364/OME.9.000663.

[39] R. J. O. Mossanek, M. Abbate, Optical response of metallic and insulating VO_2 calculated with the LDA approach, Journal of Physics: Condensed Matter 19 (2007) 346225. doi:10.1088/0953-8984/19/34/346225.

[40] J. N. Hilfiker, N. Hong, S. Schoeche, Mueller matrix spectroscopic ellipsometry, Advanced Optical Technologies 11 (2022) 59–91. doi:10.1515/aot-2022-0008.

[41] C. Wan, Z. Zhang, D. Woolf, C. M. Hessel, J. Rensberg, J. M. Hensley, Y. Xiao, A. Shahsafi, J. Salman, S. Richter, Y. Sun, M. M. Qazilbash, R. Schmidt-Grund, C. Ronning, S. Ramanathan, M. A. Kats, Optical properties of thin-film vanadium dioxide from the visible to the far infrared, Annalen der Physik 531 (2019) 1900188. doi:10.1002/andp.201900188.

Highlights

Optical anisotropy of nanostructured vanadium dioxide thermochromic thin films synthesized by reactive magnetron sputtering combined with glancing angle deposition

G. Savorianakis, C. Rousseau, Y. Battie, A. En Naciri, B. Maes, M. Voué, S. Konstantinidis

- High purity anisotropic and thermochromic VO_2 nanostructured thin films, including tilted and pillar-like morphologies, were prepared by GLAD technique
- These tilted and pillar-like morphologies markedly enhance the thermochromic behaviour of the films
- Optical characterization using azimuthal Mueller matrix measurements reveals a strong correlation between nanostructure geometry and optical anisotropy
- Finite element simulations and modelling approaches such as the Berreman 4x4 transfer matrix method provide valuable insights into the behaviour of these nanostructures.

Declaration of interests

☒ The authors declare that they have no known competing financial interests or personal relationships that could have appeared to influence the work reported in this paper.

☐ The authors declare the following financial interests/personal relationships which may be considered as potential competing interests: